

# First observation of two-neutrino double electron capture in $^{124}\text{Xe}$ with XENON1T

E. Aprile,<sup>1</sup> J. Aalbers,<sup>2,3</sup> F. Agostini,<sup>4</sup> M. Alfonsi,<sup>5</sup> L. Althueser,<sup>6</sup> F. D. Amaro,<sup>7</sup> M. Anthony,<sup>1</sup> V. C. Antochi,<sup>2</sup> F. Arneodo,<sup>8</sup> L. Baudis,<sup>9</sup> B. Bauermeister,<sup>2</sup> M. L. Benabderrahmane,<sup>8</sup> T. Berger,<sup>10</sup> P. A. Breur,<sup>3</sup> A. Brown,<sup>9</sup> A. Brown,<sup>3</sup> E. Brown,<sup>10</sup> S. Bruenner,<sup>11</sup> G. Bruno,<sup>8</sup> R. Budnik,<sup>12</sup> C. Capelli,<sup>9</sup> J. M. R. Cardoso,<sup>7</sup> D. Cichon,<sup>11</sup> D. Coderre,<sup>13</sup> A. P. Colijn,<sup>3</sup> J. Conrad,<sup>2</sup> J. P. Cussonneau,<sup>14</sup> M. P. Decowski,<sup>3</sup> P. de Perio,<sup>1</sup> P. Di Gangi,<sup>4</sup> A. Di Giovanni,<sup>8</sup> S. Diglio,<sup>14</sup> A. Elykov,<sup>13</sup> G. Eurin,<sup>11</sup> J. Fei,<sup>15</sup> A. D. Ferella,<sup>2</sup> A. Fieguth,<sup>6,\*</sup> W. Fulgione,<sup>16,17</sup> A. Gallo Rosso,<sup>16</sup> M. Galloway,<sup>9</sup> F. Gao,<sup>1</sup> M. Garbini,<sup>4</sup> L. Grandi,<sup>18</sup> Z. Greene,<sup>1</sup> C. Hasterok,<sup>11</sup> E. Hogenbirk,<sup>3</sup> J. Howlett,<sup>1</sup> M. Iacovacci,<sup>19</sup> R. Itay,<sup>12</sup> F. Joerg,<sup>11</sup> B. Kaminsky,<sup>13,†</sup> S. Kazama,<sup>9,‡</sup> A. Kish,<sup>9</sup> G. Koltman,<sup>12</sup> A. Kopec,<sup>20</sup> H. Landsman,<sup>12</sup> R. F. Lang,<sup>20</sup> L. Levinson,<sup>12</sup> Q. Lin,<sup>1</sup> S. Lindemann,<sup>13</sup> M. Lindner,<sup>11</sup> F. Lombardi,<sup>15</sup> J. A. M. Lopes,<sup>7,§</sup> E. López Fune,<sup>21</sup> C. Macolino,<sup>22</sup> J. Mahlstedt,<sup>2</sup> A. Manfredini,<sup>9,12</sup> F. Marignetti,<sup>19</sup> T. Marrodán Undagoitia,<sup>11</sup> J. Masbou,<sup>14</sup> D. Masson,<sup>20</sup> S. Mastroianni,<sup>19</sup> M. Messina,<sup>8</sup> K. Micheneau,<sup>14</sup> K. Miller,<sup>18</sup> A. Molinaro,<sup>16</sup> K. Morá,<sup>2</sup> M. Murra,<sup>6</sup> J. Naganoma,<sup>16,23</sup> K. Ni,<sup>15</sup> U. Oberlack,<sup>5</sup> K. Odgers,<sup>10</sup> B. Pelssers,<sup>2</sup> R. Peres,<sup>7,9</sup> F. Piastra,<sup>9</sup> J. Pienaar,<sup>18</sup> V. Pizzella,<sup>11</sup> G. Plante,<sup>1</sup> R. Podvianiuk,<sup>16</sup> N. Priel,<sup>12</sup> H. Qiu,<sup>12</sup> D. Ramírez García,<sup>13</sup> S. Reichard,<sup>9</sup> B. Riedel,<sup>18</sup> A. Rizzo,<sup>1</sup> A. Rocchetti,<sup>13</sup> N. Rupp,<sup>11</sup> J. M. F. dos Santos,<sup>7</sup> G. Sartorelli,<sup>4</sup> N. Šarčević,<sup>13</sup> M. Scheibelhut,<sup>5</sup> S. Schindler,<sup>5</sup> J. Schreiner,<sup>11</sup> D. Schulte,<sup>6</sup> M. Schumann,<sup>13</sup> L. Scotto Lavina,<sup>21</sup> M. Selvi,<sup>4</sup> P. Shagin,<sup>23</sup> E. Shockley,<sup>18</sup> M. Silva,<sup>7</sup> H. Simgen,<sup>11</sup> C. Therreau,<sup>14</sup> D. Thers,<sup>14</sup> F. Toschi,<sup>13</sup> G. Trincherio,<sup>17</sup> C. Tunnell,<sup>18</sup> N. Upole,<sup>18</sup> M. Vargas,<sup>6</sup> O. Wack,<sup>11</sup> H. Wang,<sup>24</sup> Z. Wang,<sup>16</sup> Y. Wei,<sup>15</sup> C. Weinheimer,<sup>6</sup> D. Wenz,<sup>5</sup> C. Wittweg,<sup>6,¶</sup> J. Wulf,<sup>9</sup> J. Ye,<sup>15</sup> Y. Zhang,<sup>1</sup> T. Zhu,<sup>1</sup> and J. P. Zopounidis<sup>21</sup>

(XENON Collaboration)\*\*

<sup>1</sup>Physics Department, Columbia University, New York, NY 10027, USA

<sup>2</sup>Oskar Klein Centre, Department of Physics, Stockholm University, AlbaNova, Stockholm SE-10691, Sweden

<sup>3</sup>Nikhef and the University of Amsterdam, Science Park, 1098XG Amsterdam, Netherlands

<sup>4</sup>Department of Physics and Astronomy, University of Bologna and INFN-Bologna, 40126 Bologna, Italy

<sup>5</sup>Institut für Physik & Exzellenzcluster PRISMA, Johannes Gutenberg-Universität Mainz, 55099 Mainz, Germany

<sup>6</sup>Institut für Kernphysik, Westfälische Wilhelms-Universität Münster, 48149 Münster, Germany

<sup>7</sup>LIBPhys, Department of Physics, University of Coimbra, 3004-516 Coimbra, Portugal

<sup>8</sup>New York University Abu Dhabi, Abu Dhabi, United Arab Emirates

<sup>9</sup>Physik-Institut, University of Zurich, 8057 Zurich, Switzerland

<sup>10</sup>Department of Physics, Applied Physics and Astronomy, Rensselaer Polytechnic Institute, Troy, NY 12180, USA

<sup>11</sup>Max-Planck-Institut für Kernphysik, 69117 Heidelberg, Germany

<sup>12</sup>Department of Particle Physics and Astrophysics, Weizmann Institute of Science, Rehovot 7610001, Israel

<sup>13</sup>Physikalisches Institut, Universität Freiburg, 79104 Freiburg, Germany

<sup>14</sup>SUBATECH, IMT Atlantique, CNRS/IN2P3, Université de Nantes, Nantes 44307, France

<sup>15</sup>Department of Physics, University of California, San Diego, CA 92093, USA

<sup>16</sup>INFN-Laboratori Nazionali del Gran Sasso and Gran Sasso Science Institute, 67100 L'Aquila, Italy

<sup>17</sup>INFN-Torino and Osservatorio Astrofisico di Torino, 10125 Torino, Italy

<sup>18</sup>Department of Physics & Kavli Institute for Cosmological Physics, University of Chicago, Chicago, IL 60637, USA

<sup>19</sup>Department of Physics "Ettore Pancini", University of Napoli and INFN-Napoli, 80126 Napoli, Italy

<sup>20</sup>Department of Physics and Astronomy, Purdue University, West Lafayette, IN 47907, USA

<sup>21</sup>LPNHE, Sorbonne Université, Université Paris Diderot, CNRS/IN2P3, Paris 75252, France

<sup>22</sup>LAL, Université Paris-Sud, CNRS/IN2P3, Université Paris-Saclay, F-91405 Orsay, France

<sup>23</sup>Department of Physics and Astronomy, Rice University, Houston, TX 77005, USA

<sup>24</sup>Physics & Astronomy Department, University of California, Los Angeles, CA 90095, USA

(Dated: December 20, 2018)

Two-neutrino double electron capture (2νECEC) is a second-order Weak process with predicted half-lives that surpass the age of the Universe by many orders of magnitude [1]. Until now, indications for 2νECEC decays have only been seen for two isotopes,  $^{78}\text{Kr}$  [2, 3] and  $^{130}\text{Ba}$  [4, 5], and instruments with very low background levels are needed to detect them directly with high statistical significance [6, 7]. The 2νECEC half-life provides an important input for nuclear structure models [8–14] and its measurement represents a first step in the search for the neutrinoless double electron capture processes (0νECEC). A detection of the latter would have implications for the nature of the neutrino and give access to the absolute neutrino mass [15–17]. Here we report on the first direct observation of 2νECEC in  $^{124}\text{Xe}$  with the XENON1T Dark Matter detector. The significance of the signal is  $4.4\sigma$  and the corresponding half-life  $T_{1/2}^{2\nu\text{ECEC}} = (1.8 \pm 0.5_{\text{stat}} \pm 0.1_{\text{sys}}) \times 10^{22}$  y is the longest ever measured directly. This study demonstrates that the low background and large target mass of xenon-based Dark Matter detectors make them well suited to measuring other rare processes as well, and it highlights the broad physics reach for even larger next-generation experiments [18–20].

The long half-life of double electron capture makes it extremely rare and the process has escaped detection for decades. In the two-neutrino case ( $2\nu\text{ECEC}$ ), two protons in a nucleus simultaneously convert into neutrons by the absorption of two electrons from one of the atomic shells and the emission of two electron neutrinos ( $\nu_e$ ) [1]. After the capture of the two atomic electrons, mostly from the K shell [21], the filling of the vacancies results in a detectable cascade of X-rays and Auger electrons [22]. The nuclear binding energy  $Q$  released in the process ( $\mathcal{O}(\text{MeV})$ ) is carried away by the two neutrinos, which are not detected within the detector. Thus, the experimental signature appears in the keV-range rather than the MeV-range. The process is illustrated in Fig. 1.

$2\nu\text{ECEC}$  is allowed in the Standard Model of particle physics and related to double  $\beta$ -decay as a second-order Weak Interaction process. However, few experimental indications exist. Geochemical studies for  $^{130}\text{Ba}$  [4, 5] and a direct measurement for  $^{78}\text{Kr}$  [2, 3] quote half-lives on the order of  $10^{20} - 10^{22}$  years.

Even longer timescales are expected for a hypothetical double electron capture without neutrino emission ( $0\nu\text{ECEC}$ ) [16, 17]. A detection of this decay would show that neutrinos are Majorana particles [15], i.e. their own anti-particles, and could help understanding the dominance of matter over antimatter in our Universe by means of Leptogenesis [23]. An eventual Majorana nature would give access to the absolute neutrino mass, but rely on nuclear matrix element calculations from theory. A plethora of different calculation approaches and results exist [8–

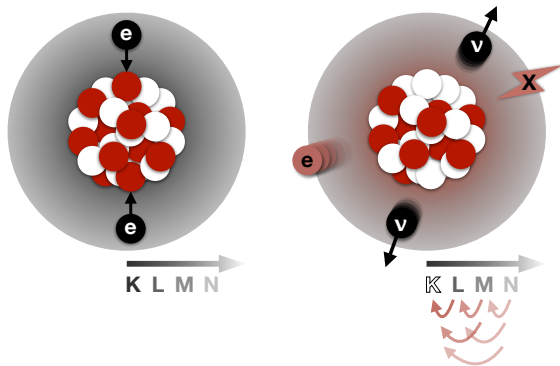


FIG. 1. In the  $2\nu\text{ECEC}$  process the nucleus captures two atomic shell electrons (black), most likely from the K-shell, and simultaneously converts two protons (red) to neutrons (white). Two neutrinos (black) are emitted in the nuclear process and carry away most of the decay energy while the atomic shell is left in an excited state with two holes in the K-shell. A cascade of X-rays (red X) and Auger electrons (red e) are emitted in the atomic relaxation where the lower shells are refilled from the higher ones (arrows).

[14]. As these models also predict the  $2\nu\text{ECEC}$  half-life, its measurement would provide necessary input to narrow down the uncertainty therein.

Here we study the  $2\nu\text{ECEC}$  of  $^{124}\text{Xe}$ . Natural xenon is a radiopure and scalable detector medium that contains about 1 kg of  $^{124}\text{Xe}$  per tonne.  $^{124}\text{Xe}$  undergoes  $2\nu\text{ECEC}$  to  $^{124}\text{Te}$  with  $Q = 2857\text{ keV}$  [24]. Since the amount of energy released by the recoiling nucleus is negligible ( $\mathcal{O}(10\text{ eV})$ ) and with the neutrinos carrying away the energy  $Q$  undetected, only the X-rays and Auger electrons are measured. The total energy for the double K-shell capture is  $64.3\text{ keV}$  [24]. This value has already been corrected for energy depositions that do not exceed the xenon excitation threshold [22, 37]. Previous searches for the  $2\nu\text{ECEC}$  decay of  $^{124}\text{Xe}$  have been carried out with gas proportional counters using enriched xenon [6] as well as large detectors originally designed for Dark Matter searches [25]. The currently leading lower limit on the half-life comes from the XMASS collaboration at  $T_{1/2}^{2\nu\text{ECEC}} > 2.1 \times 10^{22}\text{ y}$  (90% C.L.) [7].

XENON1T [26] was built to detect interactions of Dark Matter in the form of weakly interacting massive particles (WIMPs) and has recently placed the most stringent limits on the coherent elastic scattering of WIMPs with xenon nuclei [27]. XENON1T uses 3.2 t of ultra-pure liquid xenon (LXe), of which 2 t are within the sensitive volume of the time projection chamber (TPC): a cylinder of  $\sim 96\text{ cm}$  diameter and height with walls of highly-reflective PTFE that is instrumented with 248 photomultiplier tubes (PMTs). The TPC allows for the measurement of the scintillation (S1) and ionisation signals (S2) induced by a particle interaction – the latter by converting ionisation electrons into light by means of proportional scintillation. It provides calorimetry, 3D position reconstruction, and measures the scatter multiplicity.

The detector is shielded by the overburden due to its underground location at Laboratori Nazionali del Gran Sasso, an active water Cherenkov muon veto [28], and the liquid xenon itself. All detector materials were selected for low amounts of radioactive impurities and low radon emanation rates [29]. In addition, the anthropogenic  $\beta$ -emitter  $^{85}\text{Kr}$  was removed from the xenon inventory by cryogenic distillation [30]. The combination of material selection, active background reduction, and an inner low-background fiducial volume selection in data analysis results in an extremely low event rate. This makes XENON1T the currently most sensitive detector for  $2\nu\text{ECEC}$  searches in  $^{124}\text{Xe}$ .

The data presented here was recorded between February 2, 2017 and February 8, 2018 as part of a Dark Matter search. Details on the detector conditions and signal corrections can be found in the original publication [27]. The data quality criteria from the Dark Matter analysis were applied with the exception of those exhibiting low acceptance in the energy region of interest around  $60\text{ keV}$ . During the analysis, the data was blinded, i.e. inaccessible for

analysis, from 56 keV to 72 keV and only unblinded after the data quality criteria, fiducial volume, and background model had been fixed. Data sets acquired after detector calibrations with an external  $^{241}\text{AmBe}$  neutron source or a deuterium-deuterium-fusion neutron generator were removed in order to reduce the impact of radioactive  $^{125}\text{I}$ . It is produced by the activation of  $^{124}\text{Xe}$  during neutron calibrations and is taken out within a few days through the purification system. A pre-unblinding quantification of this removal using short-term calibration data led to a first reduction of the data set to 214.3 days. This data was used for fixing the background model. After unblinding, the long-term behaviour of  $^{125}\text{I}$  could be quantified and led to a further removal of data sets (methods). This yielded a final live time of 177.7 days.

Atomic X-rays and Auger electrons cannot be resolved individually due to their sub-millimetre range in LXe and the fast atomic processes. Thus, the experimental signature of K-shell  $2\nu\text{ECEC}$  in XENON1T is a single S1 + S2 pair. Both S1 and S2 signals are used for the analysis to achieve the optimal energy resolution [35] for the resulting peak. The energy scale around the expected signal at  $E_0 = (64.3 \pm 0.6)$  keV is calibrated using mono-energetic lines of injected calibration sources (e.g.  $^{83\text{m}}\text{Kr}$ ), neutron-activated xenon isotopes, and  $\gamma$ -rays from radioactive decays in detector materials. The energy resolution of a Gaussian peak at  $E_0$  is  $\sigma/\mu = (4.1 \pm 0.4)\%$  (methods). The uncertainty on  $E_0$  reflects the uncertainties of both the energy reconstruction and the correction for sub-excitation quanta. An ellipsoidal 1.5t inner fiducial mass was identified as providing the optimal signal-to-background ratio in sideband studies between 80 keV and 140 keV, above the blinded signal region.

Understanding the measured energy spectrum is essential when searching for a small peak from  $2\nu\text{ECEC}$ . Three classes of backgrounds contribute to the spectrum: intrinsic radioactive isotopes that are mixed with the LXe, radioactive isotopes in the detector materials, and solar neutrinos. The latter is subdominant and well-constrained from solar and nuclear physics.  $\gamma$ -rays from  $^{60}\text{Co}$ ,  $^{40}\text{K}$ , as well as from  $^{238}\text{U}$  and  $^{232}\text{Th}$  decay chains constitute the bulk of the material backgrounds. They can undergo forward Compton scattering before entering the 2.0t active mass and produce a flat spectrum at low energies. Multiple scatters inside the active volume are rejected by selecting events with only a single S2 compatible with a single S1. The most important intrinsic background components are  $\beta$ -decays of  $^{214}\text{Pb}$ , a daughter of  $^{222}\text{Rn}$  that is emanated from inner surfaces in contact with xenon, the two-neutrino double  $\beta$ -decay of  $^{136}\text{Xe}$ , and the  $\beta$ -decay of  $^{85}\text{Kr}$ . Mono-energetic peaks from  $^{83\text{m}}\text{Kr}$  injected for calibration and activation peaks that occur after neutron calibrations ( $^{131\text{m}}\text{Xe}$  and  $^{129\text{m}}\text{Xe}$ ) are present in the spectrum as well. The activation  $^{124}\text{Xe} + n \rightarrow ^{125}\text{Xe} + \gamma$  has implications for  $2\nu\text{ECEC}$  search as  $^{125}\text{Xe}$  decays to  $^{125}\text{I}$  via electron capture. With

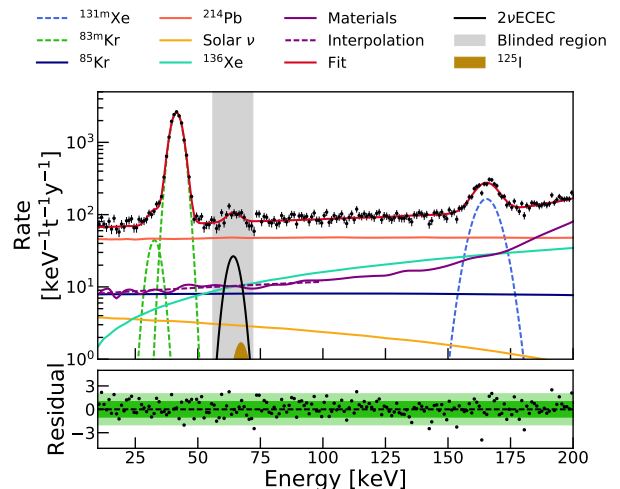


FIG. 2. Measured background energy spectrum in the 1.5 t inner fiducial mass, in which the signal-to-background ratio was found to be optimal. The data is described by a simultaneous fit of Monte Carlo generated background spectra, taking into account all known background sources and the  $2\nu\text{ECEC}$  signal (solid red line,  $\chi^2/\text{d.o.f.} \approx 527.3/462$ ). The linear interpolation of material backgrounds below 100 keV is indicated as the purple dashed line. The energy region around the expected  $2\nu\text{ECEC}$  peak was blinded (grey band) until the background model was defined. The lower panel shows the residuals between the data and the fit including  $1\sigma$  ( $2\sigma$ ) bands in green (light green).

a branching ratio of 100% and a half-life of 59.4 d,  $^{125}\text{I}$  decays into an excited state of  $^{125}\text{Te}$ . The subsequently emitted  $\gamma$ -ray together with the K-shell X-ray, which is produced in 87.5% of all cases, leads to a mono-energetic peak at 67.3 keV. Due to its proximity to  $E_0$  it would present a major background for the  $2\nu\text{ECEC}$  search that would only become apparent after unblinding. Using an activation model based on the parent isotope, we verified that  $^{125}\text{I}$  is removed from the detector with a time constant of  $\tau = (9.1 \pm 2.6)$  d (methods). This is in accordance with the continuous xenon purification using hot zirconium getters [26]. Accounting for artificial neutron activation from calibrations and for activation by radiogenic thermal neutrons in the purification loop outside the water tank, we expect  $N_{125\text{I}} = (10 \pm 7)$  events in the full data set.

The background model was constructed by matching Monte Carlo (MC) simulations of all known background components [18] with the measured energy spectrum. Taking into account the finite detector resolution, events with single energy depositions in the active volume were selected from the MC data and convolved with the measured energy resolution. The weighted sum of all spectra was optimised simultaneously to resemble the measured energy spectrum (methods). The blinded signal region was not used in the fit. The measured energy spectrum with the best fits for the individual components is shown

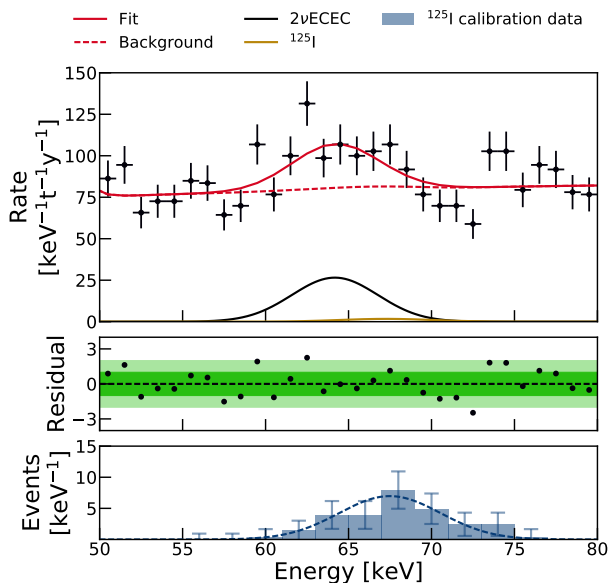


FIG. 3. Zoom on the energy region of interest for  $2\nu\text{ECEC}$  in  $^{124}\text{Xe}$ . The best fit contribution from  $2\nu\text{ECEC}$  with  $N_{2\nu\text{ECEC}} = 126$  events is given by the solid black line while the full fit is indicated as the solid red line. The peak from  $^{125}\text{I}$  with  $N_{^{125}\text{I}} = 9$  events is indicated by the solid gold line. The background-only model without  $2\nu\text{ECEC}$  (red dashed) clearly does not describe the data. Residuals for the best fit are given in the central panel with the  $1\sigma$  ( $2\sigma$ ) band indicated in green (light green). The bottom panel shows a histogram of the  $^{125}\text{I}$  activation peak as seen in 6 d of data after a dedicated neutron generator calibration. A linear background has been subtracted from the data and the peak shows the expected shift with respect to the  $2\nu\text{ECEC}$  signal.

in Fig. 2. After unblinding of the signal region a clear peak at  $E_0$  was identified. The energy and signal width obtained from the spectral fit to the unblinded data are  $\mu = (64.2 \pm 0.5)$  keV and  $\sigma = (2.6 \pm 0.3)$  keV, respectively. The resulting sum spectrum of the event rate is shown in Fig. 3. Converting the fit to a total event count yields  $N_{^{125}\text{I}} = (9 \pm 7)$  events from the decay of  $^{125}\text{I}$  and  $N_{2\nu\text{ECEC}} = (126 \pm 29)$  events from  $2\nu\text{ECEC}$ . Compared to the null hypothesis the  $\sqrt{\Delta\chi^2}$  of the best-fit is 4.4.

Several consistency checks have been carried out. It was verified that the signal is homogeneously distributed in space and we checked that the signal accumulates linearly with the exposure. A simultaneous fit of an inner (1.0 t) and outer (0.5 t) detector mass with different background compositions yielded consistent signal rates. We verified the linearity of the energy calibration by identifying the  $^{125}\text{I}$  activation peak at its expected position, which is separated from  $E_0$  by more than the energy resolution.

The fit accounts for systematic uncertainties such as cut acceptance and the number of  $^{125}\text{I}$  events by including them as fit parameter constraints. Additional systematics have to be considered when converting the ob-

served number  $N_{2\nu\text{ECEC}}$  into a half-life. The  $^{124}\text{Xe}$  isotopic abundance in XENON1T has been measured underground with a residual gas analyser (RGA) with a systematic uncertainty of 1.5%. The resulting abundance is  $\eta = (9.94 \pm 0.14_{\text{stat}} \pm 0.15_{\text{sys}}) \times 10^{-4} \frac{\text{mol}}{\text{mol}}$ , which is 4% larger than the natural abundance of  $\eta = (9.52 \pm 0.03) \times 10^{-4} \frac{\text{mol}}{\text{mol}}$  [31]. The acceptance of the data selection criteria between 55 keV and 75 keV is constant within the uncertainties at  $\epsilon = 0.967 \pm 0.007_{\text{stat}} \pm 0.033_{\text{sys}}$ . The additional systematic uncertainty accounts for the fact that for a few data selection criteria only a lower limit on the acceptance was measurable. The finite resolution of the position reconstruction in XENON1T leads to an uncertainty on the fiducial mass. This was quantified by contrasting the mass fraction, derived from the fiducial volume geometry and LXe density of  $2.862 \text{ g/cm}^3$  at  $-96.1^\circ\text{C}$  [32], with the fraction of  $^{83\text{m}}\text{Kr}$  events in the fiducial volume. With this, the fiducial mass is  $m = (1502 \pm 9_{\text{sys}})$  kg. The half-life is then calculated as

$$T_{1/2}^{2\nu\text{ECEC}} = \ln(2) \frac{\epsilon \eta N_A m t}{M_{\text{Xe}} N_{2\nu\text{ECEC}}},$$

where  $M_{\text{Xe}}$  is the mean molar mass of xenon,  $N_A$  is Avogadro's constant, and  $t$  is the live-time of the measurement. The resulting half-life for the K-shell double electron capture of  $^{124}\text{Xe}$  is  $T_{1/2}^{2\nu\text{ECEC}} = (1.8 \pm 0.5_{\text{stat}} \pm 0.1_{\text{sys}}) \times 10^{22}$  y. This is the longest half-life ever measured directly. Indications for a similarly-long half-life for  $2\nu\text{ECEC}$  decay were reported for  $^{78}\text{Kr}$  [3]. Within the uncertainties the half-lives are equally long, but the uncertainty of our new result for  $^{124}\text{Xe}$  is about two times smaller. Furthermore, the result is compatible with the lower limit from XMASS [7].

This first direct observation of  $2\nu\text{ECEC}$  in  $^{124}\text{Xe}$  illustrates how xenon-based Dark Matter search experiments, with their ever-growing target masses and simultaneously decreasing background levels, are becoming relevant for other rare event searches and neutrino physics. It sets the stage for  $0\nu\text{ECEC}$  searches that can complement double  $\beta$ -decay experiments in the hunt for the Majorana neutrino. Related processes involving the emission of one or two positrons ( $2\nu\text{EC}\beta^+$ ,  $2\nu\beta^+\beta^+$ ,  $0\nu\text{EC}\beta^+$ ,  $0\nu\beta^+\beta^+$ ) in  $^{124}\text{Xe}$  might also exhibit interesting experimental signatures. The next generation detectors XENONnT [18], LZ [19] and PandaX-4T [33] are already around the corner and will be able to probe these yet unobserved decays with unprecedented sensitivity.

## METHODS

**Selection of the fiducial mass.** Since the  $2\nu\text{ECEC}$  signal is proportional to the number of  $^{124}\text{Xe}$  nuclei, it grows linearly with the xenon mass of the volume selected for the analysis  $m_{\text{volume}}$ . The ability to distinguish signal events from background depends on the background uncertainty  $\Delta N_{\text{background}}$ . For a counting experiment, the uncertainty on the number of background events  $N_{\text{background}}$  is of Poissonian nature, so one has  $\Delta N_{\text{background}} = \sqrt{N_{\text{background}}}$ . The discovery sensitivity in a detector volume  $S_{\text{vol}}$  is then proportional to the xenon mass in the selected volume divided by the background uncertainty:

$$S_{\text{vol}} \propto \frac{m_{\text{volume}}}{\sqrt{N_{\text{background}}}}. \quad (1)$$

The  $S_{\text{vol}}$  parameter was optimised using an automated algorithm that tests both cylindrical and superellipsoidal volumes. A 1502-kg-mass superellipsoid was found to give the optimal sensitivity. As the signal region was blinded, the optimisation was carried out in an energy sideband from 80 keV to 140 keV. For the fit of Monte Carlo simulations to the measured energy spectrum and consistency checks, the volume was segmented into an inner and outer volume (as indicated in Fig. 4). Intrinsic background sources mixed with the xenon, solar neutrinos, and  $2\nu\text{ECEC}$  signal are expected to show the same activity in both volumes. However, the contribution from material backgrounds is strongest near the outer surface of the volumes. Fitting both volumes simultaneously gives a more robust fit and higher sensitivity than a single monolithic volume.

**Energy calibration and resolution.** Mono-energetic lines from the  $\gamma$ -decays of four different isotopes are used for the energy calibration of the XENON1T detector.  $^{83\text{m}}\text{Kr}$  is a gaseous calibration source that is homogeneously distributed inside the detector [34]. The isomer undergoes a multi-step decay that is highly converted and deposits 41.5 keV inside the detector. This represents the lowest mono-energetic calibration point. The metastable  $^{131\text{m}}\text{Xe}$  (163.9 keV) and  $^{129\text{m}}\text{Xe}$  (236.2 keV) are neutron-activated during calibration campaigns and decay with half-lives of 11.86 d and 8.88 d, respectively. The 1173.2 keV and 1332.5 keV transitions of  $^{60}\text{Co}$ , which is present in the stainless steel detector components such as the cryostat, are the highest energy calibration lines. Only energy depositions where the total energy of the  $\gamma$ -transition is deposited in a single resolvable interaction within the detector are taken into account, i.e. the full absorption peak. The S1 and S2 signals from these interactions are then used to determine the yields of light and charge per unit energy for each source. The two

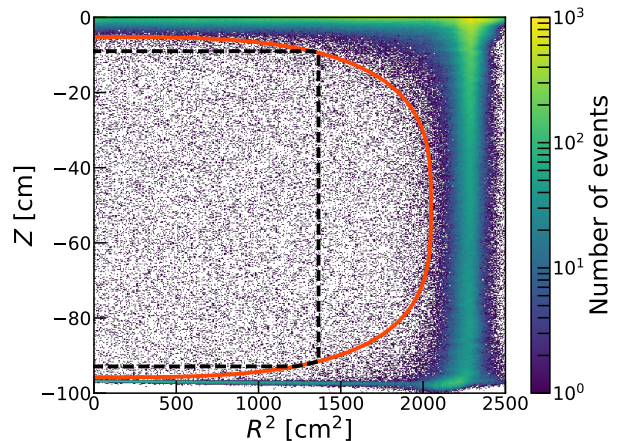


FIG. 4. Spatial distribution in interaction depth  $z$  vs. squared radius  $R^2$  of events in a 80 keV-140 keV window. High density areas correspond to the edges of the TPC where the majority of external  $\beta$ - and  $\gamma$ -radiation is absorbed. The 1502 kg fiducial volume is indicated by the solid red line. The further segmentation into an inner (1.0 t) and outer (0.5 t) volume is marked by the black dashed line.

quantities are anti-correlated [36], resulting in:

$$E = W \cdot \left( \frac{cS1}{g_1} + \frac{cS2_b}{g_2} \right) \quad (2)$$

at a given energy  $E$ . Here,  $W = (13.7 \pm 0.2)$  eV [37] is the average energy needed to generate measurable quanta in LXe (S1 photons or S2 electrons), and  $cS1$  and  $cS2_b$  are the measured S1 and S2 signals corrected for detector-effects. S1 is corrected for the spatially dependent S1 light collection efficiency, whereas S2 is corrected for the spatial dependencies of both the charge amplification and the S2 light collection efficiency. The subscript on  $cS2_b$  identifies the S2 signal seen by the bottom PMT array that is used for energy reconstruction in order to minimise the impact of signal saturation and non-uniformity due to single inactive PMTs in the top array. A fit to the measured data points gives the detector-specific calibration parameters  $g_1$  and  $g_2$ . The calibration procedure is carried out in ten slices along the central axis of the cylindrical detector, in order to account for the depth dependence of  $g_1(z)$  and  $g_2(z)$  for the energy reconstruction.

The energy resolution is determined from the reconstructed spectrum by fitting Gaussian functions with the mean  $\mu_E$  and standard deviation  $\sigma_E$  to mono-energetic peaks of the calibration sources ( $^{83\text{m}}\text{Kr}$ ,  $^{131\text{m}}\text{Xe}$ ,  $^{129\text{m}}\text{Xe}$ ) and radioactive isotopes in the TPC materials ( $^{214}\text{Pb}$ ,  $^{208}\text{Tl}$ ) up to 510.8 keV. The relative resolution is then given by  $\sigma_E/\mu_E$  for each peak. The data points are finally fitted with a phenomenological function

$$\frac{\sigma_E}{\mu_E} = \frac{a}{\sqrt{E}} + b, \quad (3)$$

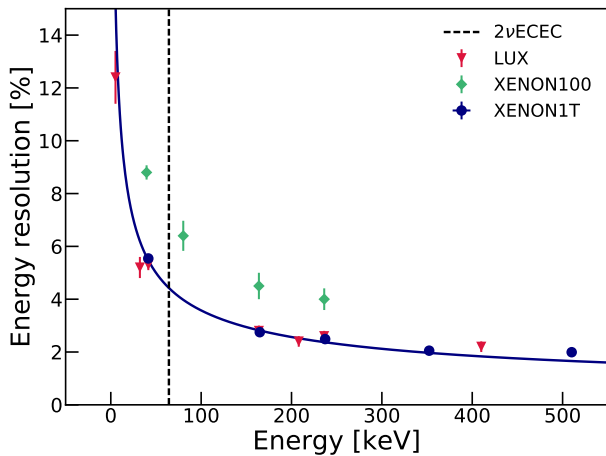
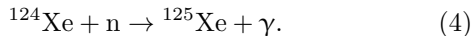


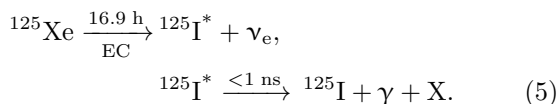
FIG. 5. Energy resolution of low energy mono-energetic lines for selected liquid xenon Dark Matter experiments [38, 39] and the XENON1T detector in the 1.5 tonne fiducial mass. The relative resolution is defined as  $\sigma_E/\mu_E$  of the Gaussian lines and fitted using a phenomenological function (solid blue line). For XENON1T the data points are  $^{83m}\text{Kr}$  (41.5 keV),  $^{131m}\text{Xe}$  (163.9 keV),  $^{129m}\text{Xe}$  (236.2 keV),  $^{214}\text{Pb}$  (351.9 keV) and  $^{208}\text{Tl}$  (510.8 keV). Only statistical uncertainties are shown for XENON1T which are too small to be visible. The energy of the  $2\nu\text{ECEC}$  peak is indicated by the black dashed line.

which gives an energy resolution of 4.1 % at the  $2\nu\text{ECEC}$  energy (Fig. 5).

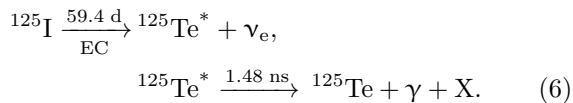
**Iodine removal.** Thermal neutrons can be captured by  $^{124}\text{Xe}$  producing  $^{125}\text{Xe}$ :



$^{125}\text{Xe}$  decays to  $^{125}\text{I}$  via electron capture with a half-life of 16.9 h:



The X-rays and Auger electrons from the atomic relaxation after the electron capture are denoted by X. Iodine also undergoes electron capture to  $^{125}\text{Te}$  with a 59.4 d half-life:



Both decays populate short-lived excited nuclear states of  $^{125}\text{I}$  and  $^{125}\text{Te}$  and the signals from the  $\gamma$ -transitions are merged with the atomic relaxation signals following the electron capture. The Te K-shell X-ray, which has a branching ratio of 87.5 %, is merged with a 35.5 keV nuclear transition. This is problematic because it makes a Gaussian line centred around 67.3 keV, which is about

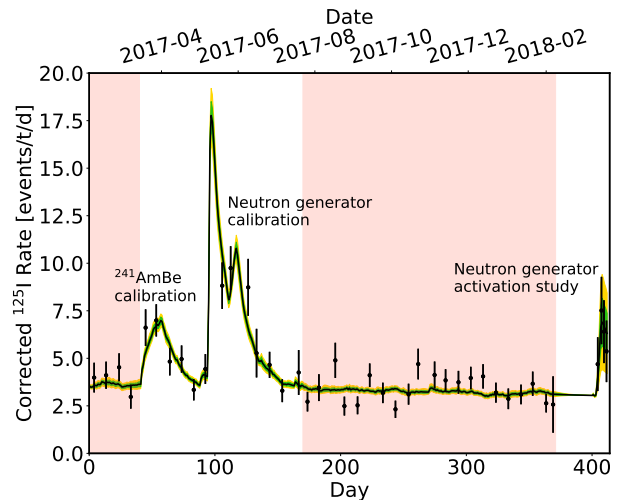


FIG. 6. Fit of the  $^{125}\text{I}$  time evolution model to data in a  $2\sigma$  interval around the  $^{125}\text{I}$  peak mean in 10-day bins. Periods with increased  $^{125}\text{I}$  decay rate are attributed to artificial activations from neutron calibrations, equipment tests, and a dedicated activation study. The decrease of the rate to the background level corresponds to an effective iodine decay constant  $\tau = 9.1$  d. The best fit is shown as the solid black line. The green (yellow) bands mark the  $1\sigma$  ( $2\sigma$ ) model uncertainties resulting from the Poisson uncertainties of the  $^{125}\text{Xe}$  data underlying the model. The data selection for the  $2\nu\text{ECEC}$  search, where the decay rate has returned to the background level, is indicated in pale red.

$1\sigma$  away from the 64.3 keV expected for  $2\nu\text{ECEC}$ .

Two significant mechanisms leading to the presence of  $^{125}\text{I}$  in the detector have been identified: artificial activation during calibration campaigns by neutrons from the deuterium-deuterium fusion neutron generator or the  $^{241}\text{AmBe}$  source, and activation outside of the water shield by environmental thermal neutrons. As the decay rate of  $^{125}\text{Xe}$  can be monitored during and after calibration campaigns, one can predict the decay rate of its iodine daughter. For environmental neutrons, flux measurements at LNGS are used to estimate the activation. These estimates are cross-checked with the  $^{125}\text{Xe}$  decay peaks in the data. In both post-AmBe and post-neutron generator data, fewer iodine decays than expected from the decay of the mother isotope  $^{125}\text{Xe}$  were found. This is attributed to the removal of  $^{125}\text{I}$  during the continuous purification of the detector's xenon inventory by circulation over hot zirconium getters. Due to the blinding of the signal region that contains the  $^{125}\text{I}$  peak, the long-term behaviour of the removal could only be assessed after unblinding.

As every  $^{125}\text{Xe}$  decay in the detector leads to the presence of an  $^{125}\text{I}$  nucleus, a model for the expected iodine decay rate from artificial activation is constructed by integrating the background-subtracted  $^{125}\text{Xe}$  rate over time in one-day steps. The data is then convolved with the effective decay constant  $\tau$  and fitted with a free ampli-

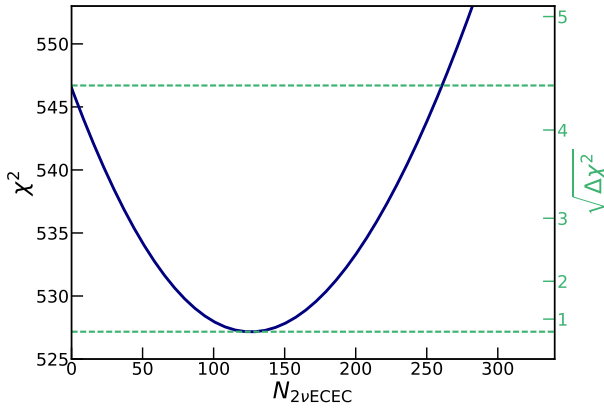


FIG. 7.  $\chi^2$  curve for the number of measured  $2\nu\text{ECEC}$  events. Comparing the best fit value of  $N_{2\nu\text{ECEC}} = 126$  events to a null result one obtains  $\sqrt{\Delta\chi^2} = 4.4$ .

tude and linear background to the measured  $^{125}\text{I}$  rate evolution in a  $2\sigma$  interval around the peak (61.7 keV to 72.9 keV). An effective  $^{125}\text{I}$  decay constant of  $\tau = (9.1 \pm 2.6)$  d was found, which is in agreement with an expected decay constant from completely efficient getter removal.

Since the model is constructed directly from data, the uncertainties from the  $^{125}\text{Xe}$  rates are propagated by introducing artificial Poisson fluctuations to the data points. An  $^{125}\text{I}$  model is made for each variation of the  $^{125}\text{Xe}$  data and fitted to the  $^{125}\text{I}$  rate evolution. The best fit to the  $^{125}\text{I}$  rate over time in 10-day bins and the uncertainty band derived from an ensemble of 1,000 fits are shown in Fig 6. Different binnings between 1 and 14 days have been tested for consistency with  $\chi^2$  and log-likelihood fits.

An integration of each model over the actual data taking periods yields an expected number of  $^{125}\text{I}$  decays  $N_{125\text{I,art}}$ . The ensemble distribution of  $N_{125\text{I,art}}$  allows to extract both a central value and uncertainties. Now, only data sets with a decay rate at the non-activated background level are selected for the  $2\nu\text{ECEC}$  search. The final data selection is shown in Fig. 6. For the spectral fit of the remaining 177.7 live days we constrain the number of expected iodine events from artificial activation  $N_{125\text{I,art}}$  using the model. We also constrain the radiogenic component  $N_{125\text{I,rad}}$  taking into account the effective decay constant  $\tau$ .

**Fit method.** The data is fitted with all known background sources, either simulated or modelled as Gaussian peaks, and the  $2\nu\text{ECEC}$  peak. The scaling parameters of the simulated Monte Carlo spectra and the properties of the Gaussian peaks are the fit parameters in a  $\chi^2$  minimisation

$$\chi_{\text{combined}}^2(\vec{p}) = \sum_i \frac{(R_i - f(E_i, \vec{p}))^2}{(\Delta R_i)^2}, \quad (7)$$

where  $R_i$  is the measured event rate in the energy bin  $E_i$  and  $f(E_i, \vec{p})$  is the background fit function. At energies below 100 keV, low statistics of simulated backgrounds from detector construction materials require an interpolation of the simulated spectra in order to avoid over-fitting. As the main background contribution from materials in this energy region are single Compton scatters from  $\gamma$ -rays in the sensitive volume, a featureless spectrum is expected. Thus, the sum of the material contributions is linearly interpolated up to 100 keV. This gives

$$f(E_i, \vec{p}) = \left[ \sum_k^{\text{materials}} p_k R_k(E_i) \right]_{\text{interpolated } < 100 \text{ keV}} + \sum_1^{\text{intrinsic}} p_1 R_1(E_i) + \sum_m^{\text{Gaussians}} \text{Gaussian}_m(\vec{p}_m, E_i), \quad (8)$$

where the sums correspond to the interpolated material component, the intrinsic sources plus solar neutrinos and the Gaussian peaks with the fit parameters  $p_{k,l,m} \in \vec{p}$ . Knowledge from external measurements, such as material screening [29],  $^{85}\text{Kr}$  concentration measurements [27] and elemental abundances have been incorporated into the fit function and are constrained using terms of the form

$$\text{constraint}_j = \frac{(\text{parameter}_j - \text{expectation}_j)^2}{\text{uncertainty}_j^2}. \quad (9)$$

A deviation of the fit parameter by  $n \times \sigma$  from the expectation will thus increase the value of the  $\chi^2$  function by  $n^2$ . The Gaussian signal peak has been constrained in the fit as well given the prior information on the expected position and width. Moreover, systematic uncertainties from the cut acceptance and fiducial mass are addressed by including these as constrained fit parameters in the fit function. As the fit is carried out in an inner and outer detector volume, each of the two volumes has its own  $\chi^2$ -function with distinct parameters for the respective fiducial masses  $\vec{V}$  and cut acceptances  $\vec{\kappa}$ . The energy reconstruction was found to agree within the uncertainties. The full  $\chi^2$  function can then be written as:

$$\begin{aligned} \chi_{\text{combined}}^2(\vec{p}, \vec{V}, \vec{\kappa}) = & \chi_{\text{inner}}^2(\vec{p}, V_{\text{inner}}, \kappa_{\text{inner}}) \\ & + \chi_{\text{outer}}^2(\vec{p}, V_{\text{outer}}, \kappa_{\text{outer}}) \\ & + \text{constraint}_{\vec{p}} \\ & + \text{constraint}_{\vec{V}} \\ & + \text{constraint}_{\vec{\kappa}}. \end{aligned} \quad (10)$$

More details of the background modelling will be discussed in a future publication.

**Fit result.** The  $\chi^2$  curve for the number of observed  $2\nu\text{ECEC}$  events is shown in Fig. 7. The  $4.4\sigma$  significance

is derived from the  $\Delta\chi^2$  between the best fit and a null result along the curve.

**Data availability.** The data that support the findings of this study is available from the corresponding authors upon reasonable request.

## ACKNOWLEDGEMENTS

We thank Javier Menéndez for sharing his expertise in the theory of double  $\beta$ -decay. We gratefully acknowledge support from the National Science Foundation, Swiss National Science Foundation, German Ministry for Education and Research, Max Planck Gesellschaft, Deutsche Forschungsgemeinschaft, Netherlands Organisation for Scientific Research (NWO), NLeSC, Weizmann Institute of Science, I-CORE, Pazy-Vatat, Initial Training Network Invisibles (Marie Curie Actions, PITNGA-2011-289442), Fundacao para a Ciencia e a Tecnologia, Region des Pays de la Loire, Knut and Alice Wallenberg Foundation, Kavli Foundation, Abeloe Graduate Fellowship, and Istituto Nazionale di Fisica Nucleare. Data processing is performed using infrastructures from the Open Science Grid and European Grid Initiative. We are grateful to Laboratori Nazionali del Gran Sasso for hosting and supporting the XENON project.

## AUTHOR CONTRIBUTIONS

The XENON1T detector was designed and constructed by the XENON Collaboration. Operation, data processing, calibration, Monte Carlo simulations of the detector and of theoretical models, and data analyses were performed by a large number of XENON Collaboration members, who also discussed and approved the scientific results. The analysis presented here was performed by a large number of XENON Collaboration members. The paper was written by A.Fi. and C.Wi. It was reviewed and edited by the collaboration and all authors approved the final version of the manuscript.

## AUTHOR INFORMATION

Author Information Reprints and permissions information is available at [www.nature.com/reprints](http://www.nature.com/reprints). The authors declare no competing financial interests. Readers are welcome to comment on the online version of the paper. Correspondence and requests for materials should be addressed either to C.Wi. ([c.wittweg@uni-muenster.de](mailto:c.wittweg@uni-muenster.de)), to A.Fi. ([a.fieguth@uni-muenster.de](mailto:a.fieguth@uni-muenster.de)) or to the XENON collaboration ([xenon@lngs.infn.it](mailto:xenon@lngs.infn.it)).

\* [a.fieguth@uni-muenster.de](mailto:a.fieguth@uni-muenster.de)

† Also at Albert Einstein Center for Fundamental Physics, University of Bern, Bern, Switzerland

‡ Also at Kobayashi-Maskawa Institute, Nagoya University, Nagoya, Japan

§ Also at Coimbra Polytechnic - ISEC, Coimbra, Portugal

¶ [c.wittweg@uni-muenster.de](mailto:c.wittweg@uni-muenster.de)

\*\* [xenon@lngs.infn.it](mailto:xenon@lngs.infn.it)

- [1] Winter, R. G. Double K Capture and Single K Capture with Positron Emission. *Phys. Rev.* **100**, 142–144 (1955).
- [2] Gavriljuk, Y. M. *et al.* Indications of  $2\nu 2K$  capture in  $^{78}\text{Kr}$ . *Phys. Rev. C* **87**, 035501 (2013).
- [3] Ratkevich, S. S. *et al.* Comparative study of the double- $k$ -shell-vacancy production in single- and double-electron-capture decay. *Phys. Rev. C* **96**, 065502 (2017).
- [4] Meshik, A. P., Hohenberg, C. M., Pravdivtseva, O. V. & Kapusta, Y. S. Weak decay of  $^{130}\text{Ba}$  and  $^{132}\text{Ba}$ : geochemical measurements. *Phys. Rev. C* **64**, 035205 (2001).
- [5] Pujol, M., Marty, B., Burnard, P. & Philippot, P. Xenon in archean barite: Weak decay of  $^{130}\text{Ba}$ , mass-dependent isotopic fractionation and implication for barite formation. *Geochimica et Cosmochimica Acta* **73**, 6834 – 6846 (2009).
- [6] Gavriljuk, Y. M. *et al.*  $2K$ -Capture in  $^{124}\text{Xe}$ : Results of Data Processing for an Exposure of 37.7 kg day. *Physics of Particles and Nuclei* **49**, 563–568 (2018).
- [7] Abe, K. *et al.* Improved search for two-neutrino double electron capture on  $^{124}\text{Xe}$  and  $^{126}\text{Xe}$  using particle identification in XMASS-I. *PTEP* **2018**, 053D03 (2018). [arXiv:1801.03251](https://arxiv.org/abs/1801.03251).
- [8] Suhonen, J. Double beta decays of  $^{124}\text{Xe}$  investigated in the QRPA framework. *J. Phys.* **G40**, 075102 (2013).
- [9] Aunola, M. & Suhonen, J. Systematic study of beta and double beta decay to excited final states. *Nucl. Phys.* **A602**, 133–166 (1996).
- [10] Singh, S., Chandra, R., Rath, P. K., Raina, P. K. & Hirsch, J. G. Nuclear deformation and the two neutrino double- $\beta$ -decay in  $^{124,126}\text{Xe}$ ,  $^{128,130}\text{Te}$ ,  $^{130,132}\text{Ba}$  and  $^{150}\text{Nd}$  isotopes. *Eur. Phys. J.* **A33**, 375–388 (2007). [arXiv:0706.4357](https://arxiv.org/abs/0706.4357).
- [11] Hirsch, M., Muto, K., Oda, T. & Klapdor-Kleingrothaus, H. V. Nuclear structure calculation of  $\beta^+\beta^+$ ,  $\beta^+\text{EC}$  and  $\text{ECEC}$  decay matrix elements. *Zeitschrift für Physik A Hadrons and Nuclei* **347**, 151–160 (1994).
- [12] Rumyantsev, O. A. & Urin, M. H. The Strength of the analog and Gamow-Teller giant resonances and hindrance of the 2 neutrino  $\beta\beta$  decay rate. *Phys. Lett.* **B443**, 51–57 (1998). [arXiv:nucl-th/9807039](https://arxiv.org/abs/nucl-th/9807039).
- [13] Pirinen, P. & Suhonen, J. Systematic approach to  $\beta$  and  $2\nu\beta\beta$  decays of mass  $A = 100 - 136$  nuclei. *Phys. Rev.* **C91**, 054309 (2015).
- [14] Pérez, E. A. C., Menéndez, J. & Schwenk, A. Two-neutrino double electron capture on  $^{124}\text{Xe}$  based on an effective theory and the nuclear shell model (2018). [arXiv:1809.04443](https://arxiv.org/abs/1809.04443).
- [15] Majorana, E. Theory of the symmetry of electrons and positrons. *Il Nuovo Cimento (1924-1942)* **14**, 171 (1937).
- [16] Bernabeu, J., De Rujula, A. & Jarlskog, C. Neutrinoless Double Electron Capture as a Tool to Measure the  $\nu_e$  Mass. *Nucl. Phys.* **B223**, 15–28 (1983).



- [17] Sujkowski, Z. & Wycech, S. Neutrinoless double electron capture: A tool to search for Majorana neutrinos. *Phys. Rev.* **C70**, 052501 (2004). arXiv:hep-ph/0312040.
- [18] Aprile, E. *et al.* Physics reach of the XENON1T dark matter experiment. *JCAP* **1604**, 027 (2016).
- [19] Mount, B. J. *et al.* LUX-ZEPLIN (LZ) Technical Design Report (2017). arXiv:1703.09144.
- [20] Aalbers, J. *et al.* DARWIN: towards the ultimate dark matter detector. *JCAP* **1611**, 017 (2016). arXiv:1606.07001.
- [21] Doi, M. & Kotani, T. Neutrinoless modes of double beta decay. *Prog. Theor. Phys.* **89**, 139–160 (1993).
- [22] Cullen, D. Program RELAX: A code designed to calculate atomic relaxation spectra of x-rays and electrons. Tech. Rep. UCRL-ID-110438, Lawrence Livermore National Laboratory, CA (United States) (1992).
- [23] Buchmüller, W., Peccei, R. & Yanagida, T. Leptogenesis as the Origin of Matter. *Annual Review of Nuclear and Particle Science* **55**, 311–355 (2005).
- [24] Nesterenko, D. A. *et al.* Double-beta transformations in isobaric triplets with mass numbers  $A=124, 130$ , and  $136$ . *Phys. Rev.* **C86**, 044313 (2012).
- [25] Aprile, E. *et al.* Search for two-neutrino double electron capture of  $^{124}\text{Xe}$  with XENON100. *Phys. Rev.* **C95**, 024605 (2017). arXiv:1609.03354.
- [26] Aprile, E. *et al.* The XENON1T Dark Matter Experiment. *Eur. Phys. J.* **C77**, 881 (2017). arXiv:1708.07051.
- [27] Aprile, E. *et al.* Dark Matter Search Results from a One Tonne  $\times$  Year Exposure of XENON1T. *Phys. Rev. Lett.* **121**, 111302 (2018).
- [28] Aprile, E. *et al.* Conceptual design and simulation of a water Cherenkov muon veto for the XENON1T experiment. *Journal of Instrumentation* **9**, P11006 (2014).
- [29] Aprile, E. *et al.* Material radioassay and selection for the XENON1T dark matter experiment. *Eur. Phys. J.* **C77**, 890 (2017).
- [30] Aprile, E. *et al.* Removing krypton from xenon by cryogenic distillation to the ppq level. *The European Physical Journal C* **77**, 275 (2017).
- [31] de Laeter, J. *et al.* Atomic weights of the elements. Review 2000 (IUPAC Technical Report). *Pure Appl. Chem.* **75**, 683 (2003).
- [32] Linstrom, P. & W.G. Mallard, E. *NIST Chemistry WebBook, NIST Standard Reference Database Number 69* (National Institute of Standards and Technology, Gaithersburg MD, 2018).
- [33] Zhang, H. *et al.* Dark matter direct search sensitivity of the PandaX-4T experiment. *Sci. China Phys. Mech. Astron.* **62**, 31011 (2019). arXiv:1806.02229.
- [34] Manalaysay, A. *et al.* Spatially uniform calibration of a liquid xenon detector at low energies using 83m-Kr. *Rev. Sci. Instrum.* **81**, 073303 (2010). arXiv:0908.0616.
- [35] Conti, E. *et al.* Correlated fluctuations between luminescence and ionization in liquid xenon. *Phys. Rev. B* **68**, 054201 (2003).
- [36] Aprile, E., Giboni, K. L., Majewski, P., Ni, K. & Yamashita, M. Observation of Anti-correlation between Scintillation and Ionization for MeV Gamma Rays in Liquid Xenon. *Phys. Rev.* **B76**, 014115 (2007). arXiv:0704.1118.
- [37] Szydagis, M. *et al.* NEST: A Comprehensive Model for Scintillation Yield in Liquid Xenon. *JINST* **6**, P10002 (2011). arXiv:1106.1613.
- [38] Akerib, D. S. *et al.* Signal yields, energy resolution, and recombination fluctuations in liquid xenon. *Phys. Rev. D* **95**, 012008 (2017).
- [39] Aprile, E. *et al.* The XENON100 Dark Matter Experiment. *Astroparticle Physics* **35**, 573 – 590 (2012).